Supporting Information

HfO_2/HfS_2 hybrid heterostructure fabricated via controllable chemical conversion of two-dimensional HfS_2

Shen Lai,[1] Seongjae Byeon,[2] Sung Kyu Jang,[1] Juho Lee,[2] Byoung Hun Lee,[3] Jin-Hong Park,[1] Yong-Hoon Kim,[2*] and Sungjoo Lee[1*]

[1]SKKU Advanced Institute of Nanotechnology (SAINT), Sungkyunkwan University, Suwon 440-746, Korea
[2]Graduate School of Energy, Environment, Water, and Sustainability, Korean Advanced Institute of Science and Technology, 291 Deahak-ro, Yuseong-gu, Daejeon 34141, Korea
[3]School of Materials Science and Engineering, Gwangju Institute of Science and Technology, Gwangju 500-712, Korea

Contents

Table S1. Summary of mobility values for HfS_2 channel FETs. Note that HfS_2 flakes in all below works are all prepared with same approach (mechanical exfoliation) to make fair comparison.

References	Contact materials	Mobility (cm^2/Vs)	On/Off ratio
This work	Graphene	1-10	10^7
Ref S1	Ti or Pt	0.03 (Ti), 0.0015 (Pt)	10^5
Ref S2	Au or Cr	0.05-2.4 (Au), 0.001-1 (Cr)	10^3-10^8
Ref S3	Au	0.2	10^7
Ref S4	Au	0.1	10^5

Obvious mobility improvement are observed in our work thanks to the high interface quality between HfS_2 channel and converted HfO_2 dielectric. When a FET is working, carrier transport proceeds at channel/dielectric interface, thus a high quality interface will lead to less carrier scattering and result in higher carrier mobility.[S5]

However, contact resistance also has strong influence on field effect mobility.[S6] Considering there is no contact engineering in our device, our mobility value should be much further improved after a careful contact engineering. In fact, mobility improvement from 1 cm^2/Vs to 50 cm^2/Vs in 2D $MoTe_2$ was observed with contact engineering.[S7] Assuming a similar improvement after contact engineering, mobility of our device will reach the theoretical limit value (around 100 cm^2/Vs at room temperature)[S8].

Table S2. The device performances of top-gated FETs based on the converted HfO_2/HfS_2 hybrid structure and other 2D materials with conventional deposited or transferred dielectrics.

References	Channel	Dielectric	Method	D_{it} ($cm^{-2}eV^{-1}$)	SS (mV/dec)	On/Off ratio
This work	HfS_2	15 nm HfO_2	Conversion	6×10^{11}	67	10^7
Ref S4	HfS_2	5 nm HfO_2	ALD	7×10^{13}	197	10^4
Ref S9	MoS_2	9 nm HfO_2	ALD	2.3×10^{12}	65	10^8
Ref S10	MoS_2	6 nm Al_2O_3	Transfer	2.2×10^{13}	180	10^6
Ref S11	WSe_2	Al_2O_3/Fluoropolymer	ALD	2×10^{12}	400	10^7
Ref S12	ReS_2	30 nm Al_2O_3	ALD	$>10^{13}$	750	10^6
Ref S25	MoS_2	15 nm Al_2O_3	ALD	5.7×10^{11}	69	10^6
Ref S26	MoS_2	16 nm Al_2O_3	ALD	2.4×10^{12}	140	10^5

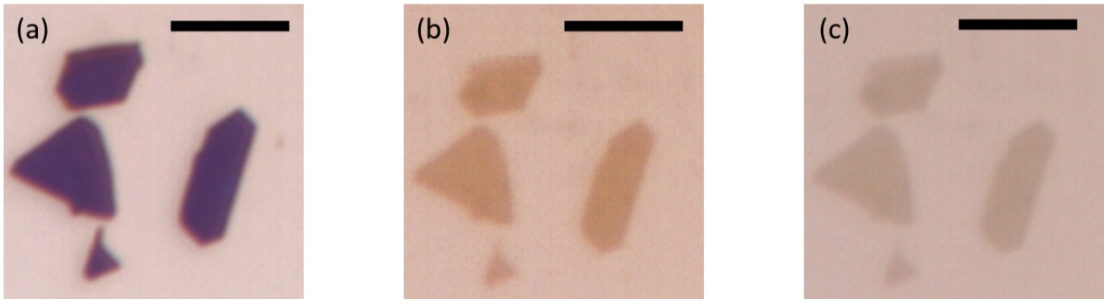

Figure S1. OM images of (a) as-exfoliated HfS_2 flakes, (b) partially converted HfO_2/HfS_2 hybrid structures and (c) fully converted HfO_2. Scale bars, 4μm.

Samples shown in Figure S1a, b and c are corresponding to the schematic diagrams in Figure 1a, b and c in main manuscript, respectively.

Partially converted HfO_2/HfS_2 hybrid structure (Figure S1b) possesses a lower contrast than as-exfoliated HfS_2 flakes (Figure S1a) because the remaining unconverted HfS_2 layers are thinner. The fully converted HfO2 flakes (Figure S1c) are almost transparent. The above observations are consistent with the optical properties of HfO_2 thin films.[S13]

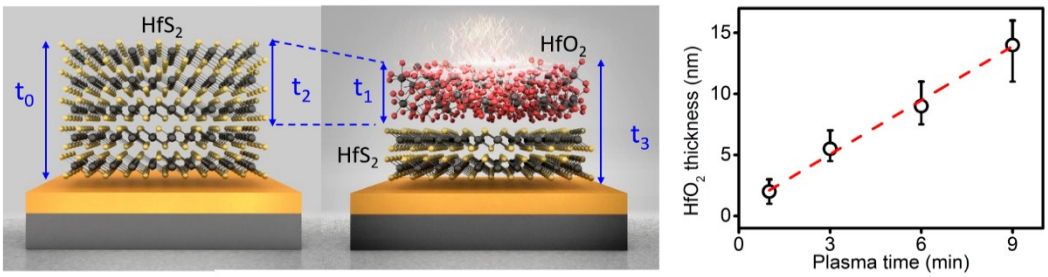

Figure S2. Rate of conversion of HfO_2 under standard plasma oxidation conditions (a power of 20 W, a flow rate of 5 sccm, a pressure of 470 mTorr).

The thickness of the converted HfO_2 layer in the converted HfO_2/HfS_2 hybrid structure cannot be directly determined with AFM because the measured thickness includes both converted HfO_2 and unconverted HfS_2. We developed an indirect approach to extract this information as presented below.

We first define several relevant parameters as indicated by the blue arrows in the above schematic

diagram.

Thickness of as-exfoliated HfS_2: t_0

Thickness of converted HfO_2: t_1

Thickness of original HfS_2 converted to HfO_2: t_2

Thickness of the converted HfO_2/HfS_2 hybrid structure: t_3

Then the quantitative relations between these parameters are as follows.

The unconverted HfS_2 in the converted HfO_2/HfS_2 hybrid structure remains intact as as-exfoliated HfS_2, so the difference between the thickness of the as-exfoliated HfS_2 (t_0) and that of the converted HfO_2/HfS_2 hybrid structure (t_3) is equal to the difference between the thickness of the original HfS_2 converted to HfO_2 (t_2) and that of the converted HfO_2 (t_1): $t_0-t_3 = t_2-t_1$.

Further, as shown in Figure 1 in the main manuscript, the thickness of original HfS_2 converted to HfO_2 (t_2) is 1.8 times the thickness of converted HfO_2 (t_1): $t_2 = 1.8\ t_1$.

Considering the above two equations ($t_0-t_3 = t_2-t_1$ and $t_2 = 1.8\ t_1$), we obtain the equation: $t_0-t_3 = 1.8t_1-t_1 = 0.8\ t_1$.

As t_0 (the thickness of the as-exfoliated HfS_2) and t_3 (the thickness of the converted HfO_2/HfS_2 hybrid structure) can be directly measured with AFM, t_1 (the thickness of converted HfO_2) can be extracted by using the above quantitative relation, and thus the thickness of the converted HfO_2 layer in the converted HfO_2/HfS_2 hybrid structure can be determined.

We further performed plasma oxidation on a thick HfS_2 flake (around 50 nm) and extracted the thickness of converted HfO_2 for a wide range (2-15 nm) within which the oxidation rate still maintains constant (1.7 nm min^{-1}). This result confirms the high controllability of our plasma oxidation process.

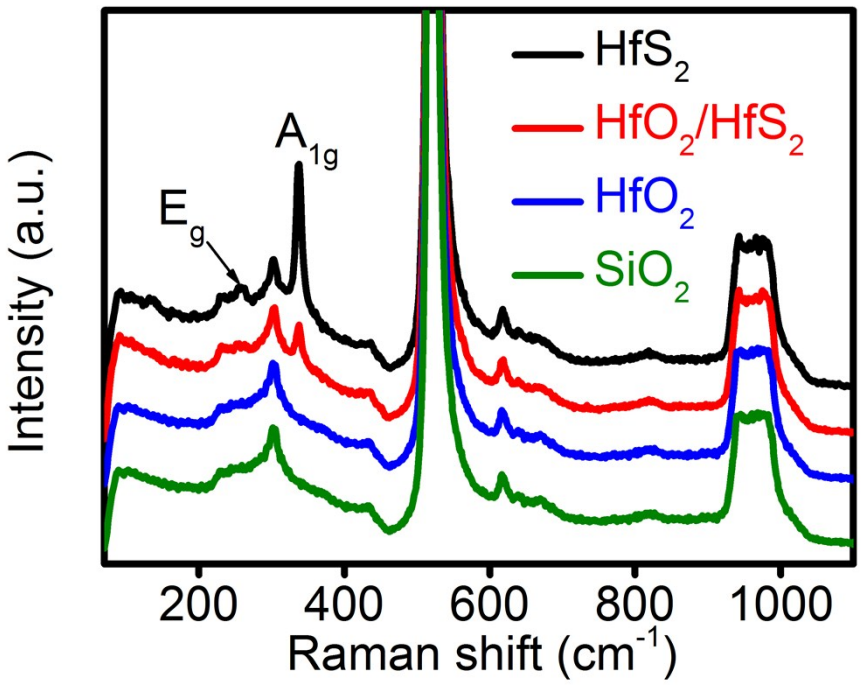

Figure S3. Wide range Raman analysis of converted HfO_2.

The Raman spectra were recorded of all samples on SiO_2/Si substrates, and the Raman spectrum of the substrate was also recorded as a reference (green curve).

The evolution of the Raman modes in these wide range (70–1100 cm^{-1}) Raman spectra through the representative stages from the original HfS_2 (black curve) to the converted HfO_2/HfS_2 hybrid structure (red curve), then to fully converted HfO_2 (blue curve), is consistent with Figure 1k.

The representative Raman modes of crystalline HfO_2 are in the range 300–700 cm^{-1}.[S14] However, the Raman spectrum of fully converted HfO_2 (blue curve) matches that of the SiO_2/Si substrate (green curve), and there are no additional peaks due to crystalline HfO_2 in the range 300–700 cm^{-1}, which indicates that the converted HfO_2 is amorphous.

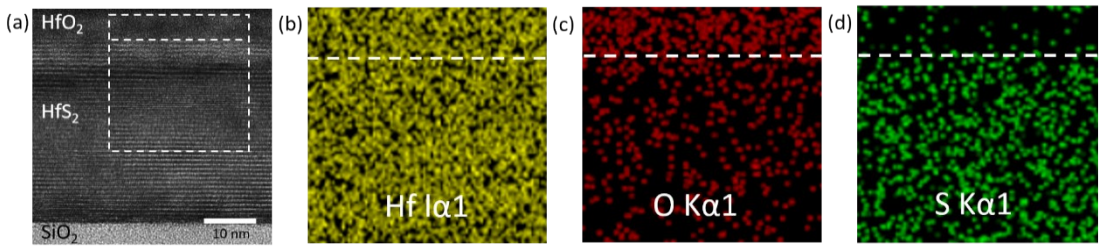

Figure S4. EDS mapping of a large-area converted HfO_2/HfS_2 hybrid structure.

To determine the cross-sectional element distribution of a converted HfO_2/HfS_2 hybrid structure, we performed EDS measurements on cross-sectional TEM samples (Figure S4a). Figures S4b-d show EDS element mapping images of the area enclosed by the white dashed lines in Figure S4a. The distributions of oxygen (Figure S4c) and sulfur (Figure S4d) are distinct in the corresponding regions of HfO_2 and HfS_2, whereas hafnium (Figure S4b) is present throughout the whole region. These distributions are consistent with the cross-sectional lattice structure in the TEM image in Figure 2 in main manuscript. Some oxygen is present in the HfS_2 region (Figure S4c) because of the ambient oxidation of HfS_2 during transfer of the sample from the FIB processing chamber to the TEM measurement chamber. Few sulfur is present in HfO_2 region due to the resolution error in EDS measurement. High resolution XPS measurements in Figure 3a in main manuscript clearly indicates a fully converted HfO_2 region without sulfur residue.

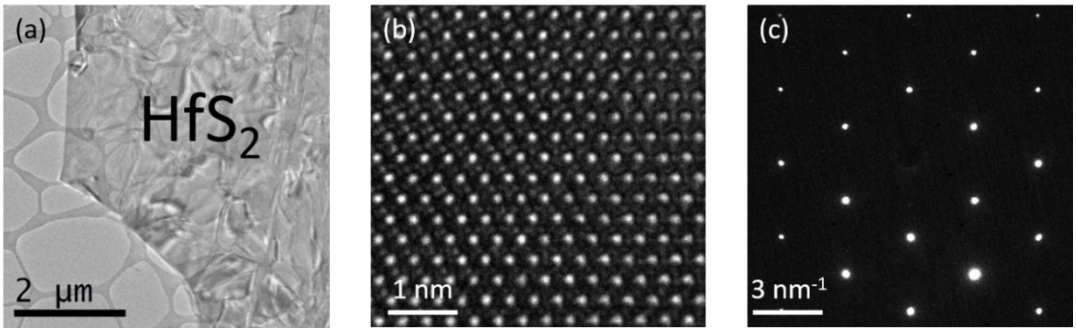

Figure S5. (a) TEM image, (b) HRTEM image, and (c) SAED pattern of a HfS_2 flake.

Figure S5a shows a low resolution TEM image of an exfoliated HfS2 flake deposited onto carbon grids inside a Cu TEM grid. HfS_2 possesses a clear hexagonal lattice structure in the HRTEM image as shown in Figure S5b, and matches well with previous reports.[S3] The selected area electron diffraction (SAED) pattern in Figure S5c indicates that the as-exfoliated HfS_2 flake is single crystalline, which is consistent with the single crystallinity of unconverted HfS_2 layers in the partially converted HfO_2/HfS_2 hybrid structure (Figure 2 in main manuscript).

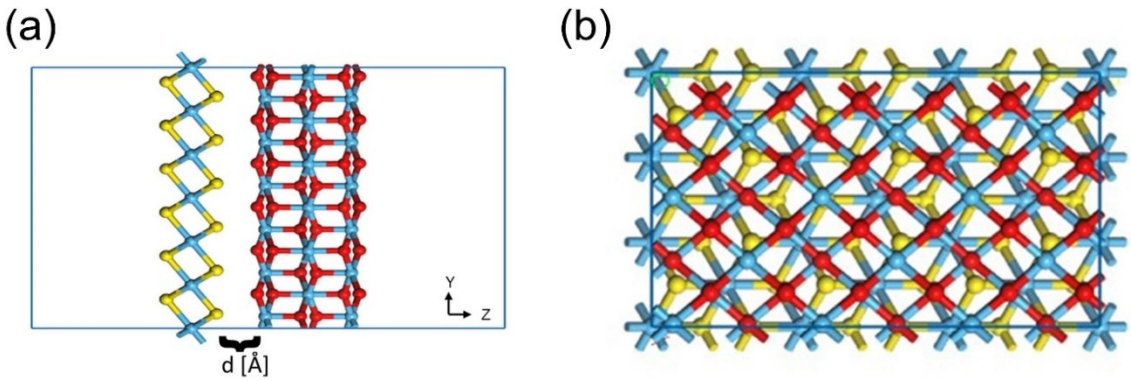

Figure S6. HfS_2 surface and HfO_2/HfS_2 interface models. (a) Side and (b) top views.

In order to prepare a computational model for the HfO_2/amorphous HfS_2 interface, we adopted a modeling procedure similar to that used for the Si/amorphous SiO_2 interface.[S15, 16] First, we adopted the monoclinic-HfO_2 (m-HfO_2) crystal structure, and by using the m-HfO_2 (001) surface, which is the prominent surface during HfO_2 growth[S17] , we evaluated the lattice mismatches between the m-HfO_2 slab and the HfS_2 monolayer for various multiples of their unit cells. Based on the calculated lattice parameters of monolayer HfS_2 (a = b = 3.607 Å) and m-HfO_2 (a = 5.142 Å, b = 5.195 Å, c = 5.326 Å), which are in agreement with previously reported values[S16, 18, 19], we prepared a HfO_2/HfS_2 heterostructure composed of a stretched (3 × 2) O-terminated m-HfO_2 (001) cell placed on top of (3 × 3 √3) monolayer HfS_2. Here, we attempted to model the experimental situation in which the deep HfS_2 layers are converted into amorphous HfO_2, so the lattice constants of the m-HfO_2 (001) slab model were scaled to those of monolayer HfS_2. For a three-layer thickness, the m-HfO_2 model consists of 72 oxygen and 36 hafnium atoms. The interlayer spacing for the optimized pristine HfS_2/HfO_2 interface model was 2.45 Å and the binding energy was −1.76 eV per S atom. A (3 × 3 √3) monolayer HfS_2 surface model was straightforwardly prepared from the interface model, and consists of 36 sulfur and 18 hafnium atoms. In both the HfS_2 surface and HfO_2/HfS_2 interface models, a vacuum space of approximately 15 Å along the surface-normal direction was included to prevent artificial interactions with periodic images.

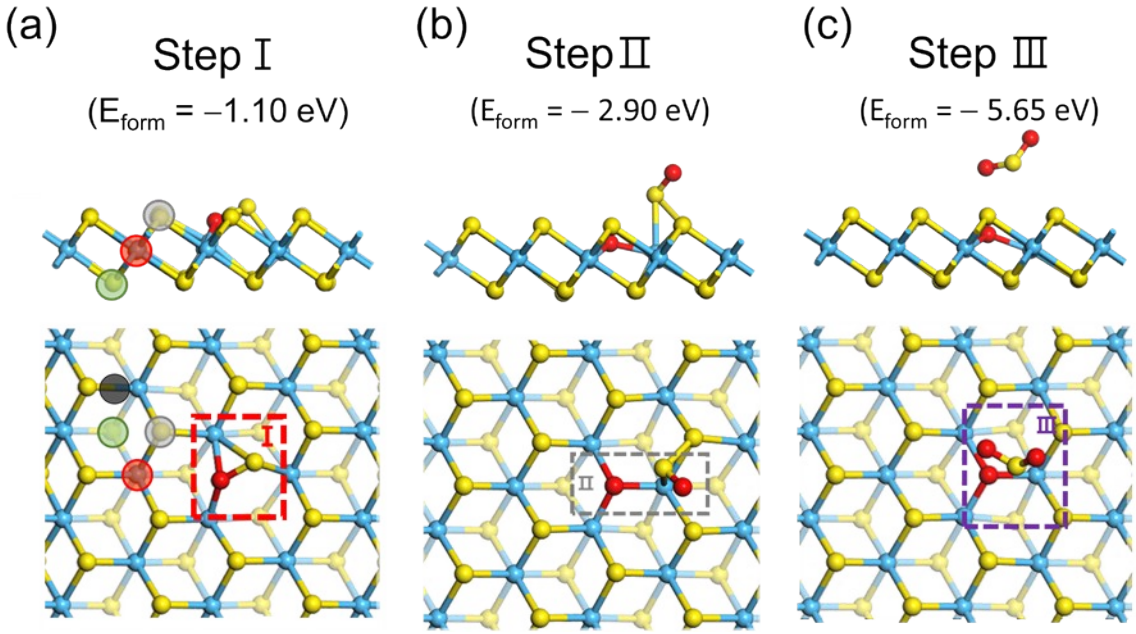

Figure S7. A plausible mechanism for the oxidation of the HfS_2 surface.

The initial oxidation of the HfS_2 basal planes can proceed easily as follows: (a) an oxygen atom penetrates into the HfS_2 surface and bonds with two hafnium atoms. Due to the penetration of the O atom, the original bonding between the S and Hf atoms will be weakened and the S atom is accordingly pushed out of the HfS_2 plane. (b) Upon the supply of an additional O atom, it will attach to the nudged-out S atom, making its bonding with the Hf atom even weaker and pulling it out further (Step II). (c) When a further O atom approaches, the S atom finally becomes disconnected from the HfS_2 region and is extracted in the form SO_2, which completes the replacement of a S atom by an O atom. In (a), the green, purple, gray, and black circles indicate the bottom-S, Hf, top-S, and top-S-Hf bridge sites, respectively, which we considered as the initial O adsorption site. Blue, yellow, and red spheres correspond to Hf, S, and O atoms, respectively.

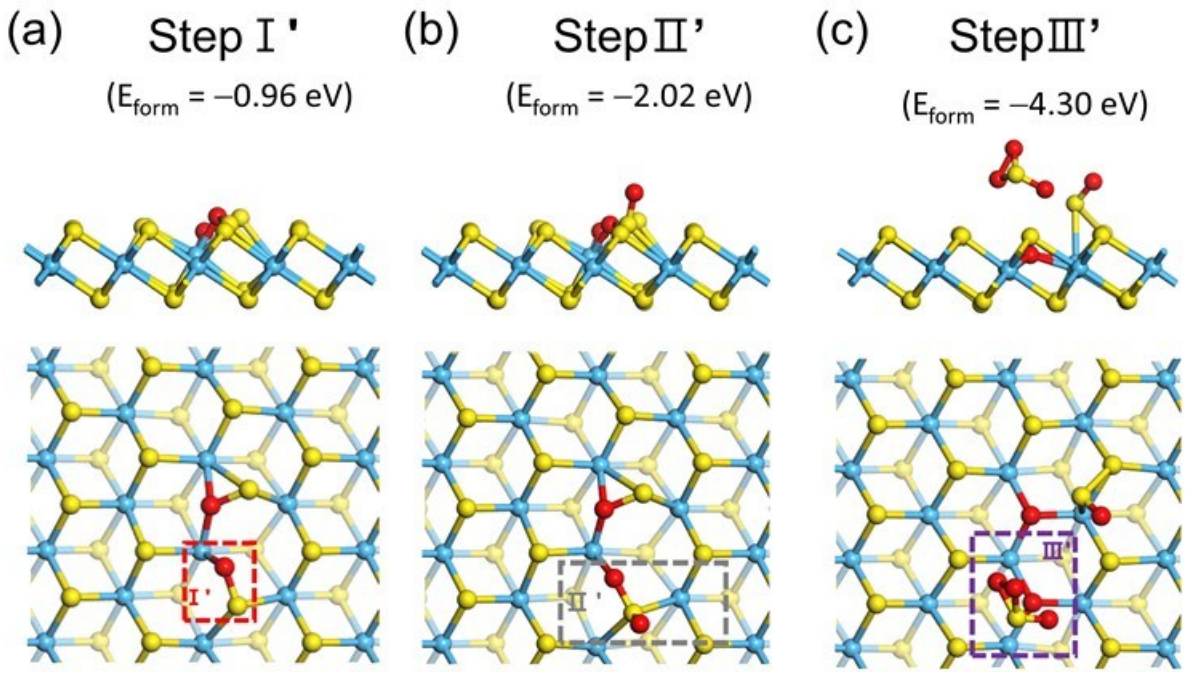

Figure S8. The mechanism of HfS_2 surface oxidation on sites next to an O atom.

We additionally confirmed that, even when an O atom is already present at a nearby site, oxidation will still proceed efficiently, with the difference that the replaced S atom is emitted as SO_3. Once an O atom has penetrated into the Hf-S bond along the armchair (zigzag) direction (Step I), another O atom can penetrate into the Hf-S bond along the neighboring zigzag (armchair) direction (Step I'), and the detachment process can occur with the continued supply of O atoms (Step I' → Step II' → Step III').

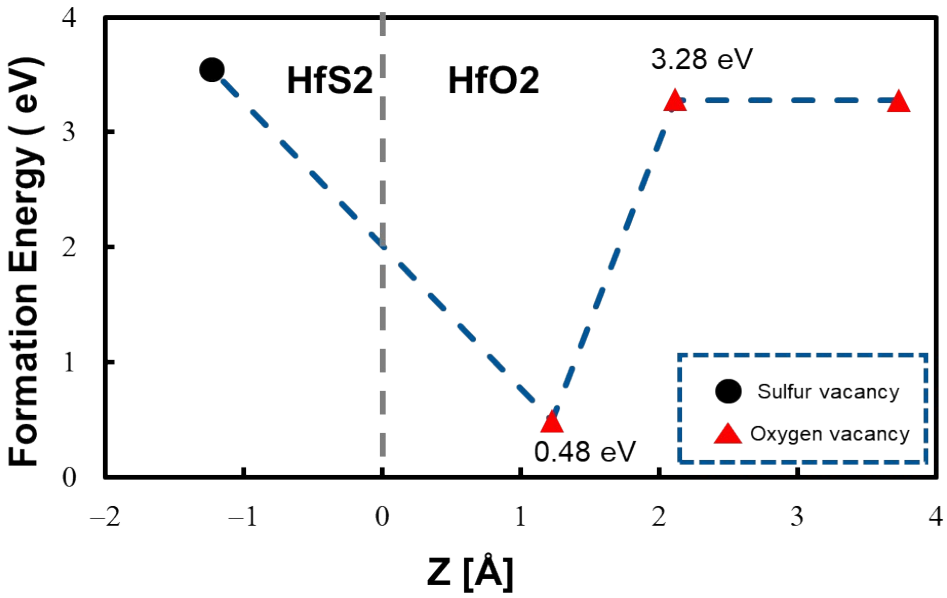

Figure S9. Formation energies of vacancy defects near the HfO_2/HfS_2 interface.

The energy cost for the formation of oxygen and sulfur vacancies in the HfO_2/HfS_2 interface model is shown as a function of the distance from the mid-point of the HfO_2/HfS_2 interfacial region (z = 0). The vacancy formation energy is defined as $E_{vac-form} = E_{vac} - E_{pristine} + n\mu_O + m\mu_S$, where E_{vac}, $E_{pristine}$, μ_O, μ_S, n, and m are the total energies of the vacancy and the pristine model for the HfO_2/HfS_2 interface structure, the chemical potentials of O and S, and the numbers of oxygen and sulfur vacancies, respectively. Comparing the energies of formation of an oxygen vacancy on the HfO_2 side (red triangles) and a sulfur vacancy on the HfS_2 side (the black circle), we conclude that the former is more favorable than the latter. In particular, we find that the oxygen vacancy at the HfO_2/HfS_2 interface region has the lowest formation energy of 0.48 eV, which is much lower than that for the deeper region of HfO_2 (3.28 eV). This indicates that the HfO_2/HfS_2 interface region will be dominated by oxygen vacancies.

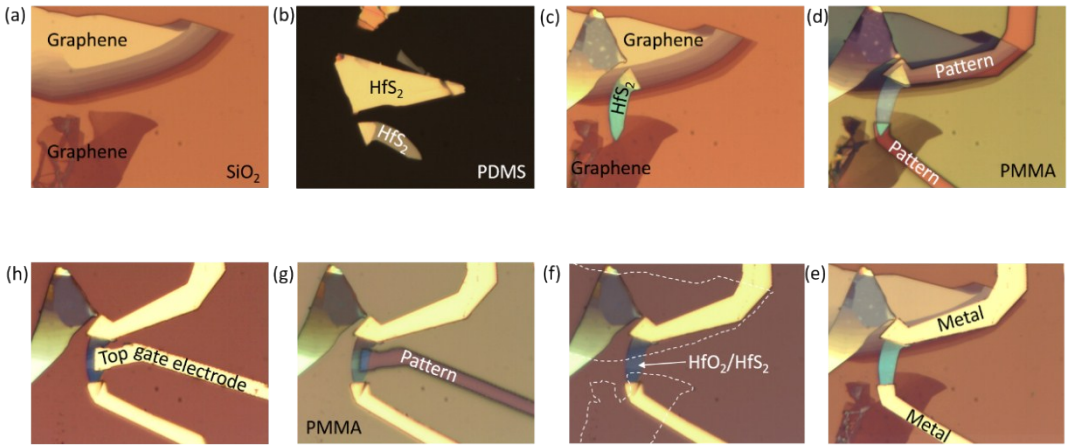

Figure S10. Detailed device fabrication process for a top-gated FET based on a converted HfO_2/HfS_2 hybrid structure. Size of OM images: 60 μm×45 μm.

Appropriate graphene flakes were exfoliated onto SiO_2 substrates as bottom source/drain electrodes and characterized with optical microscopy (Figure S10a). An HfS_2 flake (approximately 30 nm thick) was exfoliated onto a PDMS substrate and characterized with optical microscopy (Figure S10b). The HfS_2 flake was placed into contact with the graphene source/drain electrodes with a mechanical stacking process (Figure S10c).[S20] After stacking process, the HfS_2/graphene contacts were annealed in vacuum ($<10^{-6}$ Torr) at 200°C for two hours. This annealing process would enhance the contact quality, removing possible bubbles and impurities induced during the stacking process. Then the contact pads were patterned with e-beam lithography (EBL), as shown in Figure S10d. After deposition of 10 nm Cr and 50 nm Pd with e-beam evaporation, a lift-off process was conducted. The resulting HfS_2 device (Figure S10e) was treated with O_2 plasma under fixed conditions (a power of 20 W, a flow rate of 5 sccm, a pressure of 470 mTorr) for 9 min to produce a 15 nm HfO_2 layer on top of the HfS_2 channel. The exposed section of graphene was removed by the O_2 plasma, leaving the part covered by the HfS_2 flake unaffected (Figure S10f). A top gate electrode was then patterned with EBL so as to overlap the bottom graphene source/drain electrodes (Figure S10g) in order to minimize parasitic resistance. Finally, 50 nm Pd was deposited with e-beam evaporation followed by a lift-off process (Figure S10h).

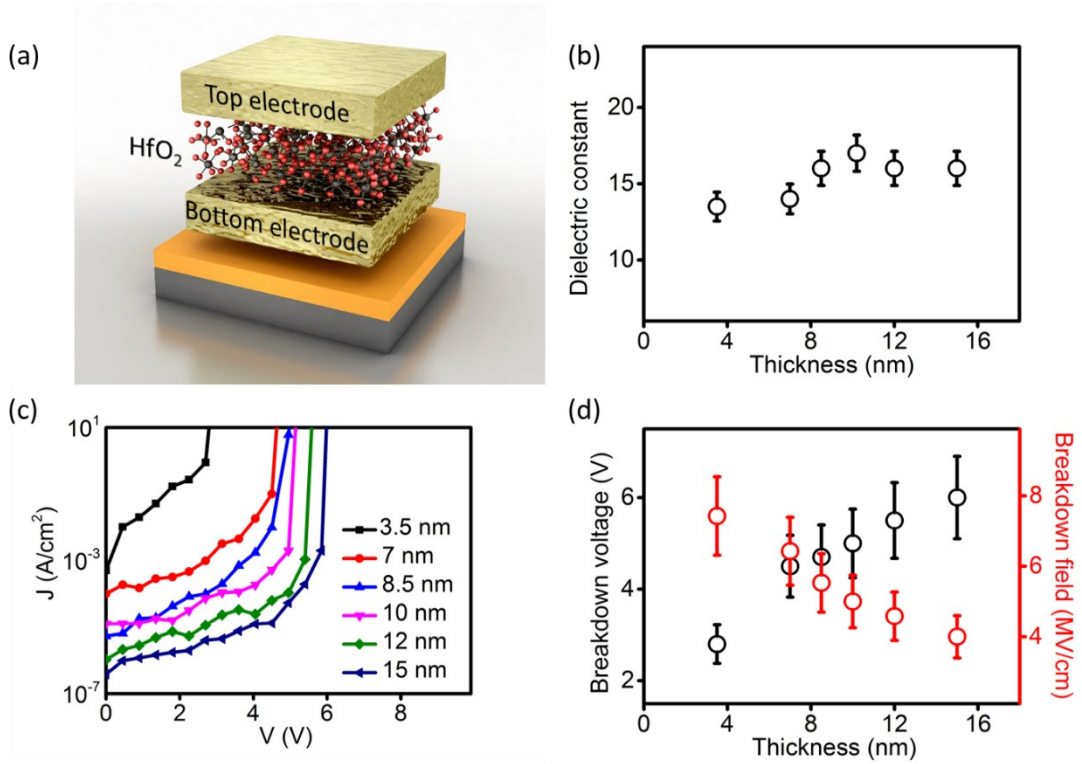

Figure S11. Dielectric properties of converted HfO_2.

Figure S11a shows a schematic diagram of a metal/converted HfO_2/metal (MIM) capacitor. The bottom electrode (Au) was fabricated by using photolithography, e-beam deposition, and a lift-off process. The base pressure of the deposition reactor was ~10^{-6} Torr. The deposition rate was ~0.1 nm/s. HfS_2 films with various thicknesses were transferred onto substrates prepared with a bottom electrode and then fully oxidized with O_2 plasma, as confirmed with Raman measurements. The same electrode (Au) preparation process was applied to prepare the top electrode.

The dielectric constants (ε_r) of the converted HfO_2 layers with various thicknesses are shown in Figure S11b. The ε_r values were extracted by using the expression $C_{ox} = \varepsilon_0\varepsilon_r/d$, where ε_0 is 8.85×10^{-14} F cm^{-1}, C_{ox} is the measured MIM capacitance, and d is the physical thickness of fully converted HfO_2, as determined with AFM. When the thicknesses of converted HfO_2 are higher than 10 nm, the dielectric constant is almost constant (15–16). When the thickness is lower than 10 nm, the dielectric constant decreases. The low dielectric constants of ultrathin HfO_2 are consistent with previous reports.[S2]

The variations with voltage of the leakage current densities at the two metal electrodes and through the converted HfO_2 layers with various thicknesses were determined and are plotted in Figure S11c. Figure S11d plots the breakdown voltage and field at which a catastrophic increase in current through the MIM capacitor was observed, as a function of the converted HfO_2 thickness. A significant increase in the breakdown voltage is evident as the converted HfO_2 thickness increases. In contrast, the breakdown electric field decreases as the converted HfO_2 thickness increases. These results are

consistent with previously reported dielectric properties of HfO_2 thin films.[S2]

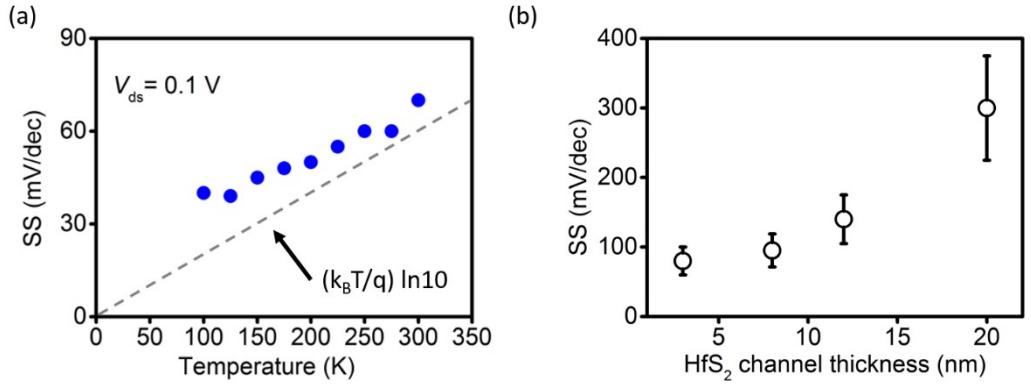

Figure S12. The variations with temperature and HfS_2 channel thickness in the SS value of a FET based on the converted HfO_2/HfS_2 hybrid structure.

Figure S12a shows the SS values of an FET with a HfS_2 channel thickness of 3 nm at various temperatures. These results show that the behavior is nearly ideal for all temperatures with a linear relationship between SS and temperature, as is consistent with the equation SS = (k_BT/q) ln10 $(1+C_{it}/C_{ox})$, which confirms a high interface quality.

The effects of varying the HfS_2 channel thickness on the device performance are shown in Figure S12b. The electrostatic control of the top gate on the HfS_2 channel decreases with the distance from the converted HfO_2/HfS_2 interface. Thus, as the HfS_2 flake thickness increases, the channel cannot be completely depleted by applying a negative V_g. Due to this effect, the SS values for devices with thicker channels are larger than those for the thinner channel device, as is evident in Figure S12b. Similar behavior has also been previously observed in MoS_2 devices.[S21]

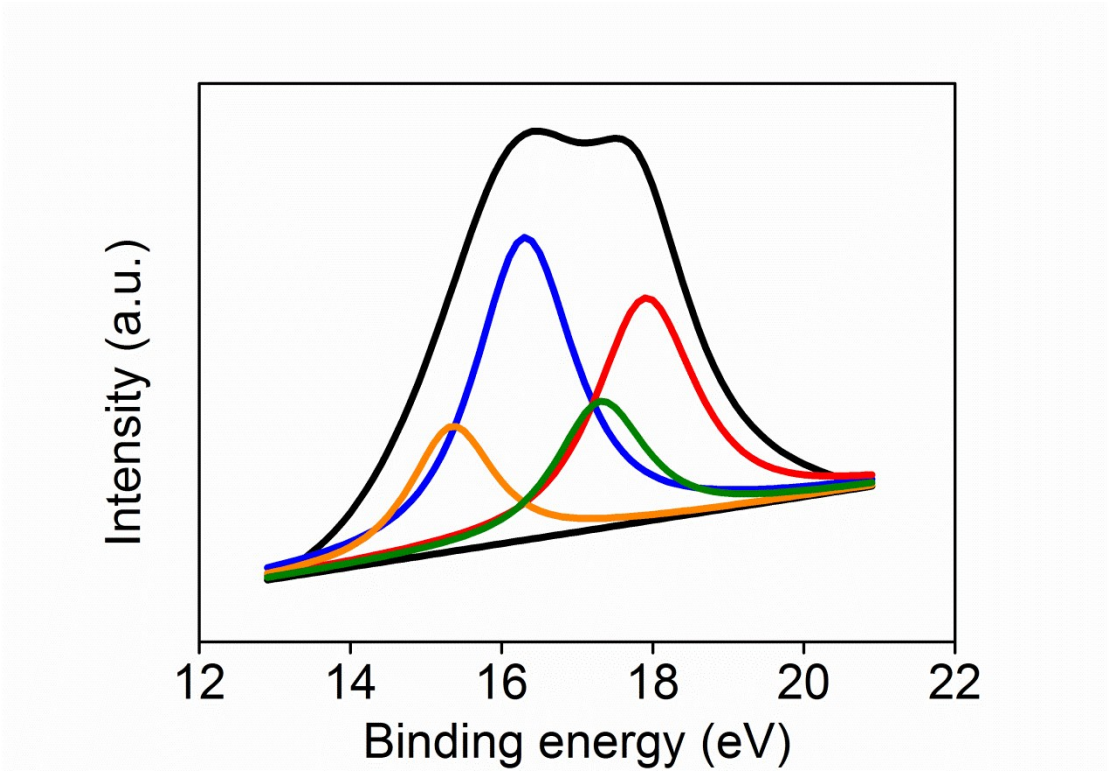

Figure S13. Deconvolution of XPS Hf 4f spectra in converted HfO_2/HfS_2 hybrid structure before argon ion sputtering treatment (P1 in Fig. 3).

FWHM of Hf $4f_{5/2}$ and Hf $4f_{7/2}$ peaks were fixed to be equal and the intensity ratio of Hf $4f_{5/2}$ peak to Hf $4f_{7/2}$ peak was found to be 74%. Other than Hf $4f_{5/2}$ at 17.9 eV (red line) and Hf $4f_{7/2}$ at 16.3 eV (blue line) of HfO_2, the Hf 4f spectra contain two peaks at 15.3 eV (orange line) and 17.3 eV (green line), which may indicate the formation of Hf-suboxide with complex chemical states that might be created during the plasma oxidation process.[S22] Although origins of these two additional peaks are not clearly understood at this moment, they should not be related to HfS_2 because no sulphur was detected in P1. For Hf 4f spectra in P2 to P5, the argon ion sputtering treatment makes it very difficult to deconvolute the spectra, as such sputtering can be sufficiently energetic which may cause further reactions.[S23, 24] A more meticulous study and analyses would be required to identify detailed chemical states of this hybrid structure.

References

S1. X. R. Nie, B. Q. Sun, H. Zhu, M. Zhang, D. H. Zhao, L. Chen, Q. Q. Sun and D. W. Zhang, *Acs Appl Mater Inter*, 2017, **9**, 26996-27003.

S2. K. Xu, Z. X. Wang, F. Wang, Y. Huang, F. M. Wang, L. Yin, C. Jiang and J. He, *Adv Mater*, 2015, **27**, 7881-7887.

S3. S. H. Chae, Y. Jin, T. S. Kirn, D. S. Chung, H. Na, H. Nam, H. Kim, D. J. Perello, H. Y. Jeong, T. H. Ly and Y. H. Lee, *Acs Nano*, 2016, **10**, 1309-1316.

S4. K. Xu, Y. Huang, B. Chen, Y. Xia, W. Lei, Z. X. Wang, Q. S. Wang, F. Wang, L. Yin and J. He, *Small*, 2016, **12**, 3106-3111.

S5. S. Kim, J. Nah, I. Jo, D. Shahrjerdi, L. Colombo, Z. Yao, E. Tutuc and S. K. Banerjee, *Appl Phys Lett*, 2009, **94**.

S6. A. Allain, J. H. Kang, K. Banerjee and A. Kis, *Nat Mater*, 2015, **14**, 1195-1205.

S7. S. Cho, S. Kim, J. H. Kim, J. Zhao, J. Seok, D. H. Keum, J. Baik, D. H. Choe, K. J. Chang, K. Suenaga, S. W. Kim, Y. H. Lee and H. Yang, *Science*, 2015, **349**, 625-628.

S8. Z. S. Huang, W. X. Zhang and W. L. Zhang, *Materials*, 2016, **9**.

S9. X. M. Zou, J. L. Wang, C. H. Chiu, Y. Wu, X. H. Xiao, C. Z. Jiang, W. W. Wu, L. Q. Mai, T. S. Chen, J. C. Li, J. C. Ho and L. Liao, *Adv Mater*, 2014, **26**, 6255-6261.

S10. W. Cao, W. Liu, J. H. Kang and K. Banerjee, *Ieee Electr Device L*, 2016, **37**, 1497-1500.

S11. S. H. H. Shokouh, P. J. Jeon, A. Pezeshki, K. Choi, H. S. Lee, J. S. Kim, E. Y. Park and S. Im, *Adv Funct Mater*, 2015, **25**, 7208-7214.

S12. E. Zhang, Y. B. Jin, X. Yuan, W. Y. Wang, C. Zhang, L. Tang, S. S. Liu, P. Zhou, W. D. Hu and F. X. Xiu, *Adv Funct Mater*, 2015, **25**, 4076-4082.

S13. M. F. Al-Kuhaili, *Opt Mater*, 2004, **27**, 383-387.

S14. S. N. Tkachev, M. H. Manghnani, A. Niilisk, J. Aarik and H. Mandar, *J Mater Sci*, 2005, **40**, 4293-4298.

S15. R. Buczko, S. J. Pennycook and S. T. Pantelides, *Phys Rev Lett*, 2000, **84**, 943-946.

S16. X. Y. Zhao and D. Vanderbilt, *Phys Rev B*, 2002, **65**.

S17. J. Aarik, A. Aidla, H. Mandar, V. Sammelselg and T. Uustare, *J Cryst Growth*, 2000, **220**, 105-113.

S18. A. B. Mukhopadhyay, J. F. Sanz and C. B. Musgrave, *Phys Rev B*, 2006, **73**.

S19. J. E. Adam, *Can Med Assoc J*, 1999, **160**, 1471-1474.

S20. T. Roy, M. Tosun, J. S. Kang, A. B. Sachid, S. B. Desai, M. Hettick, C. M. C. Hu and A. Javey, *Acs Nano*, 2014, **8**, 6259-6264.

S21. S. B. Desai, S. R. Madhvapathy, A. B. Sachid, J. P. Llinas, Q. X. Wang, G. H. Ahn, G. Pitner, M. J. Kim, J. Bokor, C. M. Hu, H. S. P. Wong and A. Javey, *Science*, 2016, **354**, 99-102.

S22. G. He, M. Liu, L. Q. Zhu, M. Chang, Q. Fang and L. D. Zhang, *Surf Sci*, 2005, **576**, 67-75.

S23. Y. Lebedinskii and A. Zenkevich, *J Vac Sci Technol A*, 2004, **22**, 2261-2264.

S24. P. K. Hurley, K. Cherkaoui, S. McDonnell, G. Hughes and A. W. Groenland, *Microelectron Reliab*, 2007, **47**, 1195-1201.

S25. P. Bolshakov, P. Zhao, A. Azcatl, P. K. Hurley, R. M. Wallace, C. D. Young, *Appl Phys Lett*, 2017, **111**, 032110.

S26. H. Liu, P. D. Ye, *IEEE Electron Device Lett*, **33**, 546-548